RSC Advances

PAPER

View Article Online
View Journal | View Issue

Cite this: *RSC Adv.*, 2025, **15**, 42364

A robust layered $Na_{0.67}Mn_{0.67}Ni_{0.33}O_2$ cathode with enhanced reversibility for sodium-ion batteries

Muhammad A. Jamali, Bauyrzhan Myrzakhmetov, Zhumabay Bakenov and Aishuak Konarov *

The development of cathode materials with high structural stability and excellent electrochemical reversibility is critical for advancing sodium-ion battery (SIB) technology. In this work, layered $Na_{0.67}Mn_{0.67}Ni_{0.33}O_2$ was synthesized *via* two distinct solid-state routes: conventional dry milling and acetone-assisted wet milling. The wet-milled approach resulted in a phase-pure layered oxide, whereas the dry-milled product exhibited minor NiO impurities. Despite this, the dry-milled sample demonstrated superior electrochemical reversibility and capacity retention compared to its phase-pure counterpart. These findings highlight the complex interplay between phase purity and functional performance, offering new insights into the optimization of sodium-ion battery cathode materials. X-ray diffraction (XRD) and transmission electron microscopy (TEM) verified the development of a well-organized layered structure, whereas scanning electron microscopy (SEM) showed evenly distributed submicron particles. Inductively coupled plasma (ICP) analysis confirmed the intended stoichiometry, while X-ray photoelectron spectroscopy (XPS) offered information on the oxidation states of Mn and Ni, strengthening the material's structural integrity. Electrochemical investigations revealed an impressive initial discharge capacity of 190 mA h g^{-1} across an extensive voltage range of 1.5–4.7 V, along with remarkable reversibility and prolonged cycling stability. The refined synthesis technique not only reduced sodium volatilization but also encouraged even elemental distribution, leading to diminished polarization and improved redox activity. The cohesive structural arrangement, uniform composition, and advantageous electrochemical characteristics solidly confirm $Na_{0.67}Mn_{0.67}Ni_{0.33}O_2$ as a strong layered oxide cathode. This study highlights the promise of optimized solid-state synthesis as an economical and scalable approach for creating next-generation SIB cathodes with enhanced stability and reversibility.

Received 15th September 2025
Accepted 24th October 2025

DOI: 10.1039/d5ra06972f

rsc.li/rsc-advances

1 Introduction

The global shift to renewable energy and electrification is creating unparalleled demand for safe, affordable, and environmentally friendly energy storage solutions.[1] Lithium-ion batteries (LIBs) presently lead this sector, fuelling consumer gadgets, electric vehicles (EVs), and more frequently, large-scale energy storage systems.[2] Their achievement is rooted in high energy density, extended cycle life, and established production facilities. Nonetheless, widespread LIB implementation encounters multiple significant obstacles. Lithium is unevenly distributed around the globe, with most reserves situated in politically unstable areas, which heightens worries about resource security, changing prices, and supply-chain risks.[3–5] Additionally, the extraction and processing of lithium require significant energy and pose environmental challenges, raising sustainability issues. Given these concerns, sodium-ion batteries (SIBs) have surfaced as a very promising alternative.[6] Sodium ranks as the sixth most plentiful element in the Earth's crust and is easily sourced from seawater and mineral deposits. In contrast to lithium, sodium is widely distributed and not limited to specific regions, providing both economic and geopolitical benefits.[7–9] Moreover, sodium possesses comparable chemical properties to lithium, facilitating the application of intercalation-based structures and, crucially, compatibility with current LIB production systems.[10] This mix of low expense, plentiful availability, and chemical resemblance makes SIBs especially appealing for stationary grid-scale applications, where affordability and sustainability of resources are frequently more important than gravimetric energy density. Even with these benefits, the commercialization of SIBs is still hindered by issues related to materials, especially concerning the cathode.[11] An optimal cathode for SIBs should exhibit high reversible capacity, swift Na^+ diffusion rates, low polarization, minimal structural deterioration during repeated cycling, and elevated coulombic efficiency.[12] Meeting these requirements has shown to be more challenging than for LIBs because of the inherent differences between lithium and sodium. Specifically,

Department of Chemical and Materials Engineering, School of Engineering and Digital Science, Nazarbayev University, 53, Kabanbay Batyr Ave., Astana, Kazakhstan. E-mail: aishuak.konarov@nu.edu.kz

the larger ionic radius of sodium ions (1.02 Å compared to 0.76 Å for Li^+) results in sluggish diffusion in solid frameworks, narrower diffusion pathways, and more severe lattice strain during insertion and extraction. These effects not only reduce rate capability but also accelerate structural instability, making the design and optimization of sodium host structures a central challenge in SIB development.[13–15] In the last ten years, various families of cathode materials have been explored for SIBs, each presenting its unique advantages and disadvantages.[16] Polyanionic substances, including phosphates, sulfates, and fluorophosphates, provide excellent structural stability and elevated operating voltages because of the robust covalent nature of the anionic groups. Nevertheless, their comparatively low electronic conductivity and constrained practical capacity limit their use.[17] Prussian blue analogues (PBAs) have attracted interest due to their open framework designs, which facilitate quick sodium-ion movement and consistent cycling. However, PBAs frequently encounter issues with crystal water inclusion, structural defects, and restricted voltage ranges, which impede their energy density.[11] Organic cathode materials signify another developing avenue, utilizing plentiful resources and adjustable redox activity. Nonetheless, their poor conductivity and solubility in electrolytes present significant obstacles to real-world implementation.[18] In this context, layered transition-metal oxides (Na_xTMO_2, TM = transition metals) are noteworthy for their high theoretical capacities, simple synthesis, and extensive tunability achieved *via* transition metal substitution. When their structural stability is meticulously managed, these oxides can provide high performance, thus becoming a key focus of SIB research.[19,20] Layered oxides can generally be classified into O3- and P2-type phases, according to sodium coordination and the stacking of oxides.[21] In O3-type structures, sodium ions reside in octahedral positions, and the stacking order adheres to an ABCABC pattern. These materials typically display elevated initial capacities but experience slow Na^+ transport because of narrow pathways and frequently undergo irreversible structural changes during cycling.[22–24] In comparison, P2-type oxides contain sodium ions in trigonal prismatic positions arranged in an ABBA stacking pattern. This arrangement creates wider diffusion channels and lower activation energies for Na^+ transport, enabling better rate capability.[25,26] However, P2-type materials are prone to voltage-driven phase transitions (such as P2-to-O2 transformations) and structural instability under deep cycling, which compromises long-term reversibility.[21] Among layered oxides, manganese-based systems (Na_xMnO_2) have been studied extensively owing to Mn's natural abundance, low cost, and environmental friendliness.[5,27,28] Manganese provides rich redox activity, contributing to high theoretical capacity. However, these materials face intrinsic challenges.[29] The presence of Mn^{3+} ions lead to Jahn–Teller distortion, which destabilizes the crystal lattice and accelerates capacity fading. Furthermore, their electronic conductivity is poor, and irreversible phase transitions during cycling often degrade performance.[30,31] To overcome these limitations, researchers have explored partial substitution of Mn with other transition metals such as Ni, Fe, Co, Ti, Cu, and V. Substitution helps mitigate Jahn–Teller distortion, stabilize the layered structure, and introduce additional redox couples for enhanced capacity.[32] Among these strategies, nickel substitution has proven particularly effective. The Ni^{2+}/Ni^{3+} redox couple contributes high-voltage capacity while simultaneously diluting Mn^{3+} ions, reducing distortion effects.[33] Nickel also improves electronic conductivity and helps stabilize the oxygen framework, both of which enhance reversibility and cycle life.[34] One particularly promising composition is $Na_{0.67}Mn_{0.67}Ni_{0.33}O_2$, a P2-type layered oxide. This stoichiometry balances high capacity, moderate redox potential, and structural robustness. However, its performance remains highly sensitive to synthesis conditions, highlighting the importance of optimizing processing parameters.[35] A variety of synthesis methods have been explored for Na-layered oxides, including sol–gel, co-precipitation, hydrothermal, spray pyrolysis, and solid-state reactions.[36] Wet-chemical methods often enable fine compositional control and uniform particle morphology but may suffer from scalability limitations, precursor costs, and phase impurities.[37] In contrast, the solid-state method offers several advantages: it is simple, low-cost, highly scalable, and readily adaptable to industrial production. Importantly, when carefully optimized, solid-state synthesis yields products with superior phase purity and robust crystallinity.[38] That said, solid-state methods also present challenges. High processing temperatures are often required, leading to sodium volatilization, while extended calcination times may cause particle coarsening.[39] Thus, meticulous control of sodium stoichiometry, heating profile, and atmosphere is essential to achieving phase-pure, electrochemically stable layered oxides.[40]

In this study, we present the optimized solid-state synthesis of $Na_{0.67}Mn_{0.67}Ni_{0.33}O_2$, targeting enhanced phase purity, structural stability, and electrochemical reversibility. A 10% sodium excess was employed to compensate for volatilization losses during high-temperature processing. A two-step heating protocol was adopted: an initial preheating stage to eliminate residual carbonates and promote inter diffusion, followed by high-temperature calcination at 950 °C to achieve well-crystallized layered structures. By combining abundant and low-cost elements (Mn, Ni, Na) with a simple, scalable synthesis route, this work contributes to bridging the gap between laboratory-scale materials development and industrial feasibility. More broadly, it underscores the importance of synthesis optimization in dictating the electrochemical performance of layered oxides. The insights gained here strengthen the case for Ni-substituted manganese oxides as practical cathodes for next-generation sodium-ion batteries and provide a pathway for further rational design of robust, high-capacity electrode materials.

2 Experimental

2.1. Materials and precursors

To synthesis the $Na_{0.67}Mn_{0.67}Ni_{0.33}O_2$, all the materials were used of analytical grade to assure the reproducibility and avoid the contamination. The sodium carbonate (Na_2CO_3, 99.5%), manganese(III) oxide (Mn_2O_3, 99%), and nickel(II) oxide (NiO, 99%) were bought from Sigma-Aldrich (USA). Super P

Conductive Carbon Black and polyvinylidene fluoride (PVDF, binder), and *N*-methyl-2-pyrrolidone (NMP, solvent) were acquired from MTI Corporation (USA) for the electrode fabrication.

2.2. Synthesis of $Na_{0.67}Mn_{0.67}Ni_{0.33}O_2$

The layered $Na_{0.67}Mn_{0.67}Ni_{0.33}O_2$ was synthesised *via* two distinct methods as illustrated in Fig. 1, firstly, for dry milled (DM) sample, the conventional solid-state reaction was followed in which all the precursors were loaded in the 80 ml jar for the Planetary Micro Mill PULVERISETTE 7 premium line in required ratios of 0.67 : 0.67 : 0.33. After assuring the jar is air tightened, precursors were milled at 700 rpm for 30–45 minutes. After milling, the precursor was pelleted into 20 mm pellets using Specac Manual Hydraulic Press. To calcinate, the pellet was placed into the alumina crucible and calcinated at 950 °C for 12 hours using Carbolite Gero Ltd muffle furnace. Similarly, for wet milled (WM) sample, acetone was introduced into the jar for uniform mixing. It was also milled for same RPM and duration. The resultant slurry was spread onto the aluminium foil and dried in the oven at 80 °C for 12 hours to remove the remaining acetone. The dried powder was then pelleted and calcinated at 950 °C for 12 hours. Resultant calcinated pellets from both methods were pulverised using Fritsch Vibratory Micro Mill Pulverisette 0 and stored into glass vials for further application.

2.3. Material characterization

The synthesised $Na_{0.67}Mn_{0.67}Ni_{0.33}O_2$ was analysed through several characterisation techniques. A Rigaku MiniFlex diffractometer (Cu Kα, λ = 1.5406 Å) was used to perform X-ray diffraction (XRD) over a 2θ range of 10°–80° in order to confirm the P2 phase and presence of any impurities. Scanning electron microscopy (SEM, Zeiss Crossbeam 540) was used to evaluate morphological features, while transmission electron microscopy (TEM) (JEOL JEM-3010) was used to look for potential flaws, stacking order, and lattice peripheries. Stoichiometry was confirmed using inductively coupled plasma optical emission spectroscopy (ICP-OES, PerkinElmer Optima 8300). Surface chemistry was examined using inductively coupled plasma optical emission spectroscopy (ICP-OES, PerkinElmer Optima 8300) with an emphasis on oxygen species and Mn and Ni oxidation states. To analyse the elemental distribution, Energy-dispersive X-ray spectroscopy (EDS) (ZEISS Crossbeam 540) was utilised.

2.4. Electrochemical characterization

To characterise the synthesised materials electrochemically, the CR2032 coin cells were assembled for which the slurry was prepared using the active material ($Na_{0.67}Mn_{0.67}Ni_{0.33}O_2$), the Super P Conductive Carbon Black and polyvinylidene fluoride (PVDF) were ground together in ratio of 80 : 10 : 10, respectively, in the presence of *N*-methyl-2-pyrrolidone (NMP). The prepared slurry was casted on aluminium foil and dried in Vacuum Ovens by Thermo Fisher Scientific at 100 °C for 12 hours. 14 mm electrodes were cut from the dried slurry and the coin cells were assembled in MBraun glovebox (O_2 and H_2O < 0.1 ppm) filled with high purity argon gas. 1 M $NaPF_6$ dissolved in propylene carbonate (PC) with 5 vol% fluoroethylene carbonate (FEC), glass fiber separators (AGM) and Na metal chip were used as electrolyte, separator and anode, respectively. The average mass loading for the electrodes for dry milled (DM) and wet milled

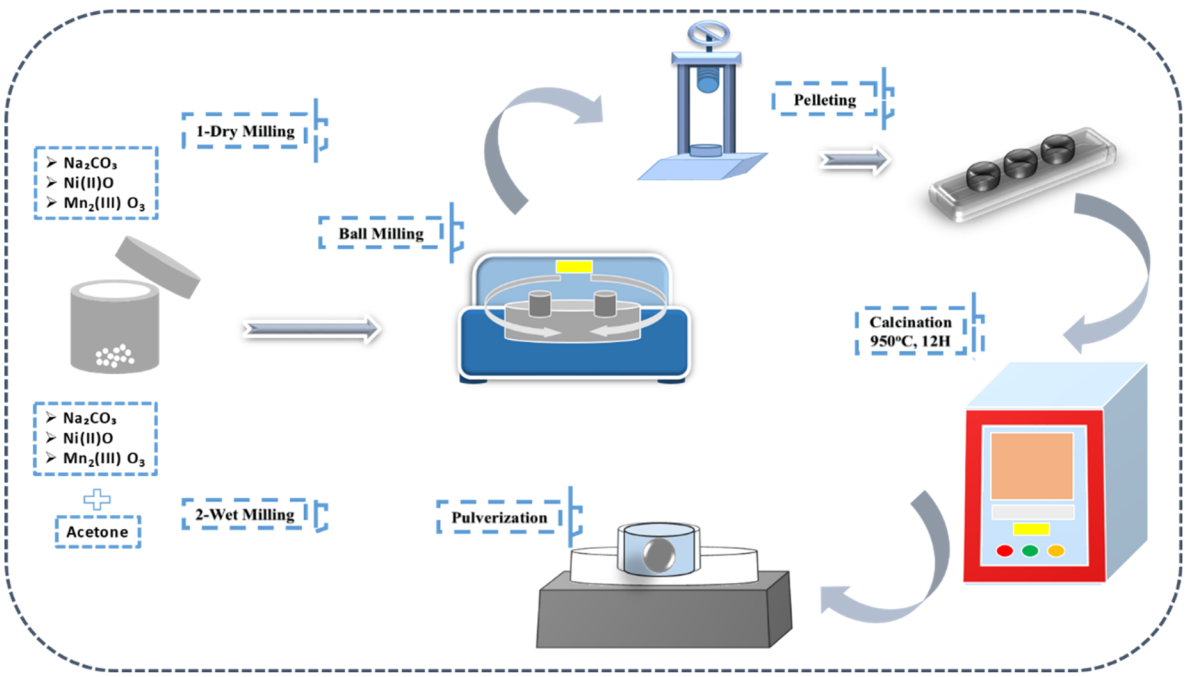

Fig. 1 Methodology for the synthesis of $Na_{0.67}Mn_{0.67}Ni_{0.33}O_2$.

(WM) methods was kept approximately to 2–2.5 mg cm^{-2}. A Neware battery testing system was subjected to galvanostatic charge–discharge (GCD) tests in voltage windows of 1.5–4.2 V, 1.5–4.5 V, and 1.5–4.7 V *vs.* Na^+/Na.

3 Results and discussion

3.1. Structural and compositional characterization

The crystal structure and compositional integrity of the as-synthesized $Na_{0.67}Mn_{0.67}Ni_{0.33}O_2$ cathode material were systematically investigated by X-ray diffraction (XRD) and inductively coupled plasma–optical emission spectroscopy (ICP-OES). The initial synthesis (Fig. 1) yielded the target layered phase, though a weak diffraction peak at ~37.2° 2θ, corresponding to NiO (PDF Card No. 04-012-6348), indicated the presence of a minor impurity. The optimization of synthesis conditions effectively removed this phase, resulting in a phase-pure sample, which is validated by the clear, distinct reflections shown in Fig. 2a. All peaks were assigned to a P2-type layered hexagonal structure with space group $P6_3/mmc$ (No. 194), closely aligning with the reference pattern for P2- $Na_{0.67}Mn_{0.67}Ni_{0.33}O_2$ (PDF Card No. 00-054-0894). The pronounced (002) reflection at ~16.5° 2θ, characteristic of layered sodium oxides, signifies ordered stacking of $[Mn,Ni]O_2$ slabs along the *c*-axis; its sharpness indicates high crystallinity and orientation, both of which are critical for facilitating fast and reversible Na^+ transport. The absence of secondary reflections further verifies the successful synthesis of a single-phase material. The atomic arrangement of the P2 framework (Fig. 2b) consists of $[MO_6]$ octahedral slabs stacked in an A–B–B–A sequence, with Na^+ occupying trigonal prismatic sites between slabs, a configuration known to provide wider diffusion channels compared to the octahedral Na^+ sites in O3-type oxides. Compositional analysis by ICP-OES confirmed a Na : Mn : Ni ratio of 0.68 : 0.66 : 0.32, in close agreement with the nominal stoichiometry, with slight sodium deficiency attributed to volatilization during high-temperature calcination. Collectively, XRD and ICP-OES confirm the successful synthesis of a phase-pure, highly crystalline P2-$Na_{0.67}Mn_{0.67}Ni_{0.33}O_2$ with well-defined layered channels, establishing its structural suitability as a promising cathode material for sodium-ion batteries.

3.2. Morphological analysis

Scanning electron microscopy (SEM) was employed to examine the surface morphology and particle distribution of the synthesized $Na_{0.67}Mn_{0.67}Ni_{0.33}O_2$ powder. Fig. 3a and b reveal that the material consists of aggregated secondary particles formed by the clustering of nanosized primary crystallites. The secondary particles are predominantly irregular in shape, with sizes ranging between 1–5 μm. The presence of angular grains with rough edges (Fig. 3a) and plate-like morphologies (Fig. 3b) indicates that the growth of crystallites is strongly influenced by the solid-state synthesis route. Such hierarchical agglomeration of nanosized crystallites into larger micrometer-sized clusters is commonly observed in P2-type layered oxides and has been reported to provide both mechanical stability and improved electronic conductivity by creating interconnected particle networks. Furthermore, the porous features and loosely packed arrangement of grains facilitate electrolyte infiltration and enhance the accessible surface area for Na^+ ion transfer during electrochemical cycling. The observed morphology therefore suggests a synergistic effect between structural stability and ion transport, which is crucial for achieving high-rate performance in sodium-ion batteries. Transmission electron microscopy (TEM) provided further insight into the crystallinity and nanoscale structure of the synthesized oxide. As shown in Fig. 3c and d, the TEM images clearly exhibit well-resolved lattice fringes with an interplanar spacing of ~0.556 nm, corresponding to the (002) plane of the layered P2-type structure. This confirms the

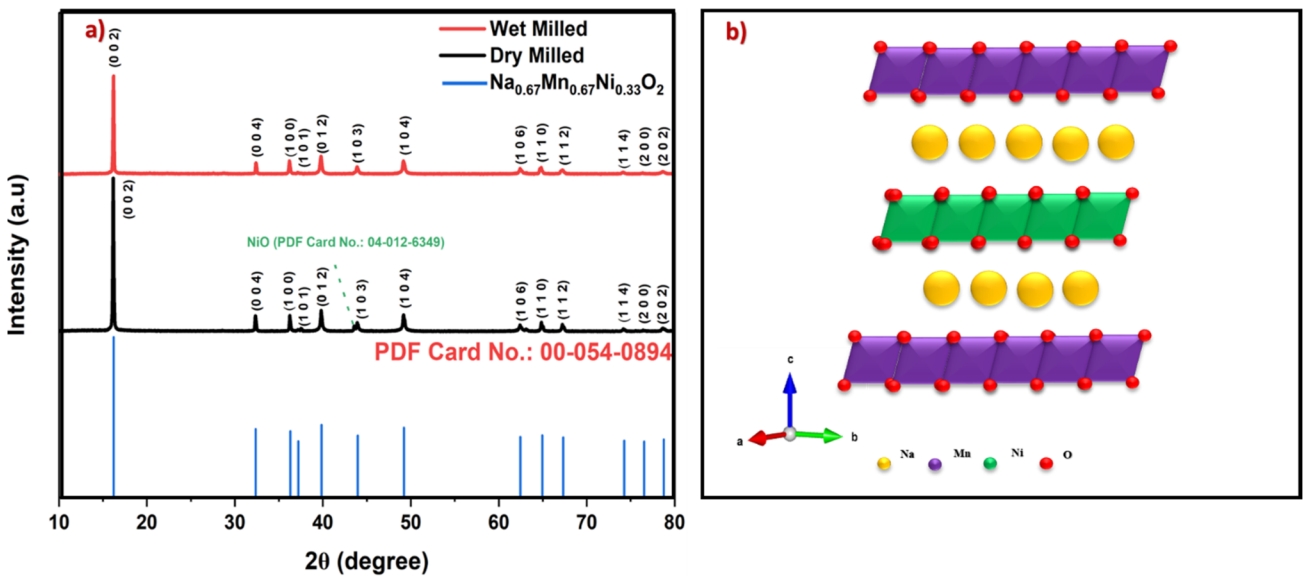

Fig. 2 Structural characterization of $Na_{0.67}Mn_{0.67}Ni_{0.33}O_2$ (a) XRD pattern. (b) P2-type crystal structure schematic.

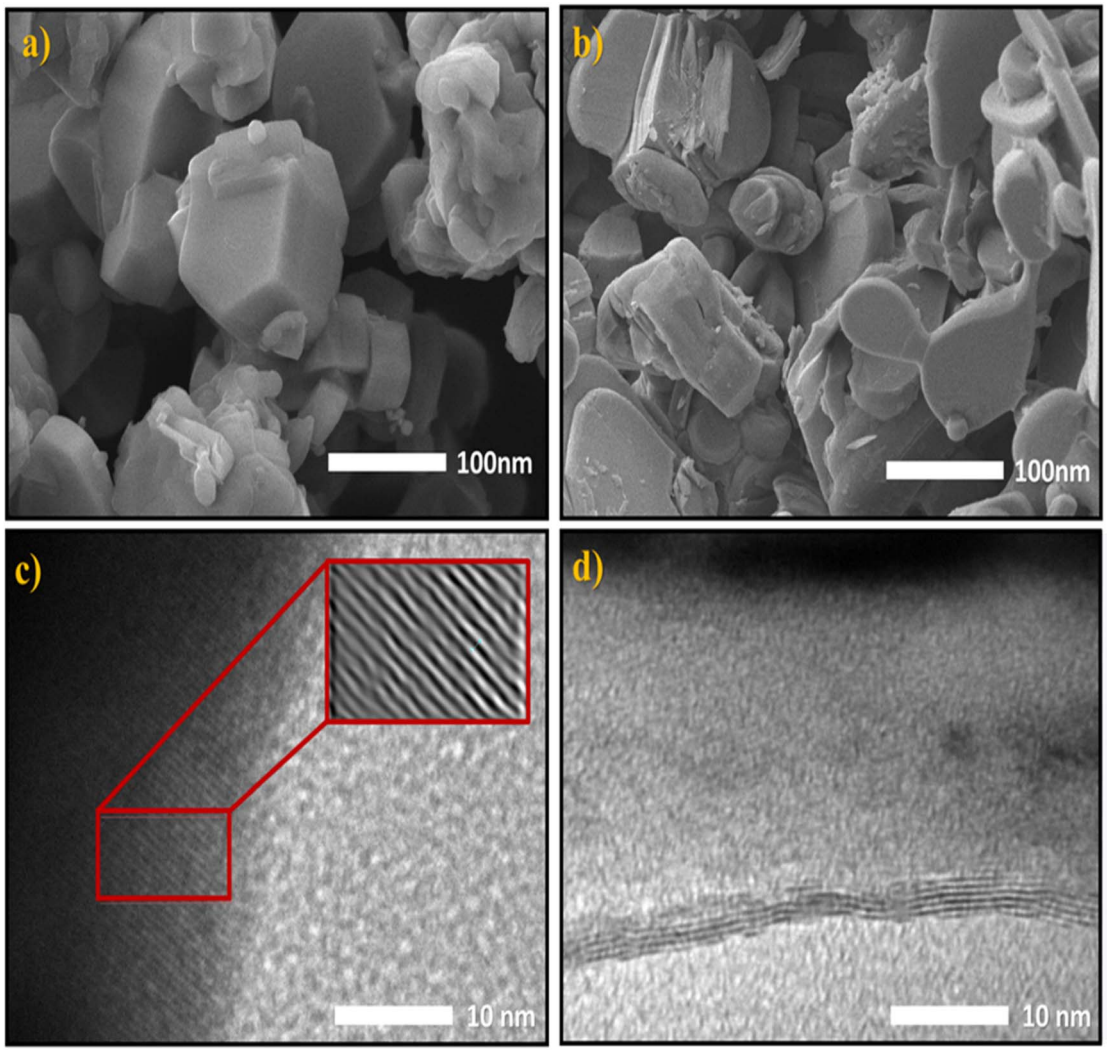

Fig. 3 SEM (a & b) and TEM (c & d) images of $Na_{0.67}Mn_{0.67}Ni_{0.33}O_2$ synthesised through solid state reaction technique.

successful formation of the characteristic prismatic sodium-ion diffusion channels along the ab-plane of the P2 framework. The regular and continuous lattice fringes with minimal dislocations or stacking defects suggest the presence of long-range ordering and high-quality crystallinity. Importantly, such crystallographic integrity is expected to contribute to stable Na^+ ion migration pathways and improved reversibility during cycling. The TEM image shown in Fig. 2d further highlights the layered arrangement of the oxide, where the parallel stacking of atomic planes can be clearly resolved. The uniform and periodic stacking without significant distortion indicates that the layered oxide structure is preserved throughout the crystallite, thereby reinforcing the structural conclusions derived from XRD. The absence of major stacking faults or amorphous regions suggests that the solid-state synthesis route successfully yielded highly crystalline layered domains. In layered transition-metal oxides, stacking faults and defects often hinder Na^+ transport and lead to capacity fading; therefore, the defect-free layered ordering observed here is advantageous for long-term cycling performance. The combined SEM, TEM, and ICP-OES analyses confirm that the synthesized $Na_{0.67}Mn_{0.67}Ni_{0.33}O_2$ cathode exhibits (i) a hierarchical microstructure of micron-sized agglomerates composed of nanosized crystallites, (ii) well-ordered P2-type layered domains with defect-free stacking, and (iii) a chemical composition closely matching the nominal stoichiometry. This optimized morphology and structure are expected to provide fast Na^+ diffusion kinetics, excellent electrode–electrolyte interfacial contact, and superior cycling stability, thereby supporting its suitability as a high-performance cathode material for sodium-ion batteries.

3.3. Surface chemistry

To obtain insight into the surface chemistry and oxidation states of the constituent elements in the $Na_{0.67}Mn_{0.67}Ni_{0.33}O_2$ cathode, X-ray photoelectron spectroscopy (XPS) was performed. The Na 1s spectrum (Fig. 4a) displays a single symmetric peak centered at ~1071.2 eV, characteristic of Na^+ ions incorporated within the oxide lattice. The O 1s region (Fig. 4e) was deconvoluted into two components: a dominant peak at ~529.6 eV attributed to lattice oxygen (O^{2-}) in the

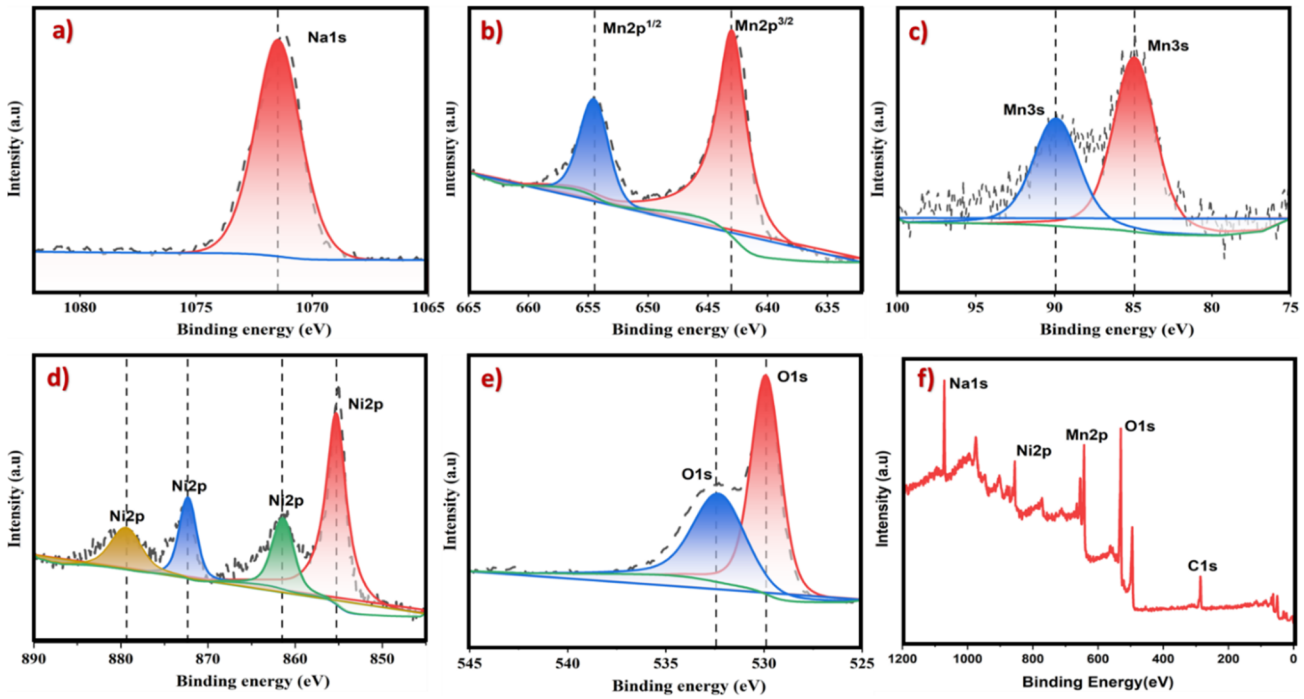

Fig. 4 X-ray photoelectron spectroscopy (XPS) analysis of $Na_{0.67}Mn_{0.67}Ni_{0.33}O_2$: (a) Na 1s spectrum, (b) Mn 2p spectrum, (c) Mn 3 s spectrum, (d) Ni 2p spectrum, (e) O 1s spectrum, and (f) survey spectrum.

[Mn,Ni]O_2 framework, confirming structural integrity, and a weaker shoulder at ~531.5 eV, corresponding to surface oxygen species such as hydroxyls or adsorbed carbonates commonly formed by ambient exposure. The Mn 2p spectrum (Fig. 4b) exhibits the expected spin–orbit doublet, with Mn $2p_{3/2}$ deconvoluted into two peaks at ~641.6 eV and ~643.0 eV, corresponding to Mn^{3+} and Mn^{4+}, respectively, thus confirming a mixed-valence state. A high fraction of Mn^{4+} is desirable, as it suppresses the Jahn–Teller distortion associated with Mn^{3+} and improves structural stability. This observation is further supported by the Mn 3 s spectrum (Fig. 4c), which shows clear multiplet splitting, with the separation energy correlating with the average Mn oxidation state and corroborating the coexistence of Mn^{3+}/Mn^{4+}. Complex characteristics may be seen in the Ni 2p spectrum (Fig. 4d), such as the Ni $2p_{3/2}$ and Ni $2p_{1/2}$ peaks with distinctive shake-up satellites. Contributions from Ni^{2+} (~854.6 eV) and Ni^{3+} (~856.5 eV) are revealed by deconvolution of the Ni $2p_{3/2}$ peak, suggesting that Ni, like Mn, exists in a mixed-valence state. This characteristic emphasizes the importance of Ni for charge correction in electrochemical cycling. The coexistence of several oxidation states (Mn^{3+}/Mn^{4+} and Ni^{2+}/Ni^{3+}) is confirmed by the XPS data taken together. These states offer synergistic redox activity, allowing for high-capacity salt storage. In the meantime, the oxide framework's resilience with little degradation is confirmed by the strong lattice oxygen signal and the comparatively weak surface-related characteristics. These findings demonstrate the strong correlation between surface chemistry and P2-$Na_{0.67}Mn_{0.67}Ni_{0.33}O_2$'s remarkable electrochemical stability. Along with a small C 1s signal resulting from inevitable adventitious carbon contamination during sample processing, the broad survey spectrum (Fig. 4f) verifies the existence of Na, Mn, Ni, and O, which is consistent with the predicted composition.

3.4. Electrochemical performance

The dry-milled $Na_{0.67}Mn_{0.67}Ni_{0.33}O_2$ cathode's electrochemical performance was thoroughly assessed *via* galvanostatic charge–discharge (GCD) cycling across various voltage ranges to determine the equilibrium between specific capacity and stability over extended cycling. When operated within the broad potential range of 1.5–4.7 V as shown in Fig. 5a, the cathode exhibited an impressive initial discharge capacity of almost 190 mA h g^{-1}, showcasing the strong Na-storage potential of the layered oxide. The GCD curves showed several voltage plateaus typical of P2-type structures, which relate to consecutive Mn^{3+}/Mn^{4+} and $Ni^{2+}/Ni^{3+}/Ni^{4+}$ redox reactions along with structural phase changes. In particular, the plateau above 4.2 V contributed substantially to the overall capacity, highlighting the role of high-voltage redox activity. However, this enhanced capacity was accompanied by pronounce instability, as reflected in the rapid capacity fading, with only ~78% of the initial capacity retained after 50 cycles as shown in Fig. 5b. Such degradation is attributed to irreversible structural transformations, possible P2–O2 phase transitions, and parasitic electrolyte decomposition triggered by the high operating potential, all of which compromise long-term reversibility. To mitigate these issues, the upper cut-off voltage was reduced to 4.0 V. Under this narrower 1.5–4.0 V window (Fig. 5c), the initial discharge capacity decreased to ~150 mA h g^{-1} because the high-voltage contribution was excluded. Nonetheless, the cycling performance

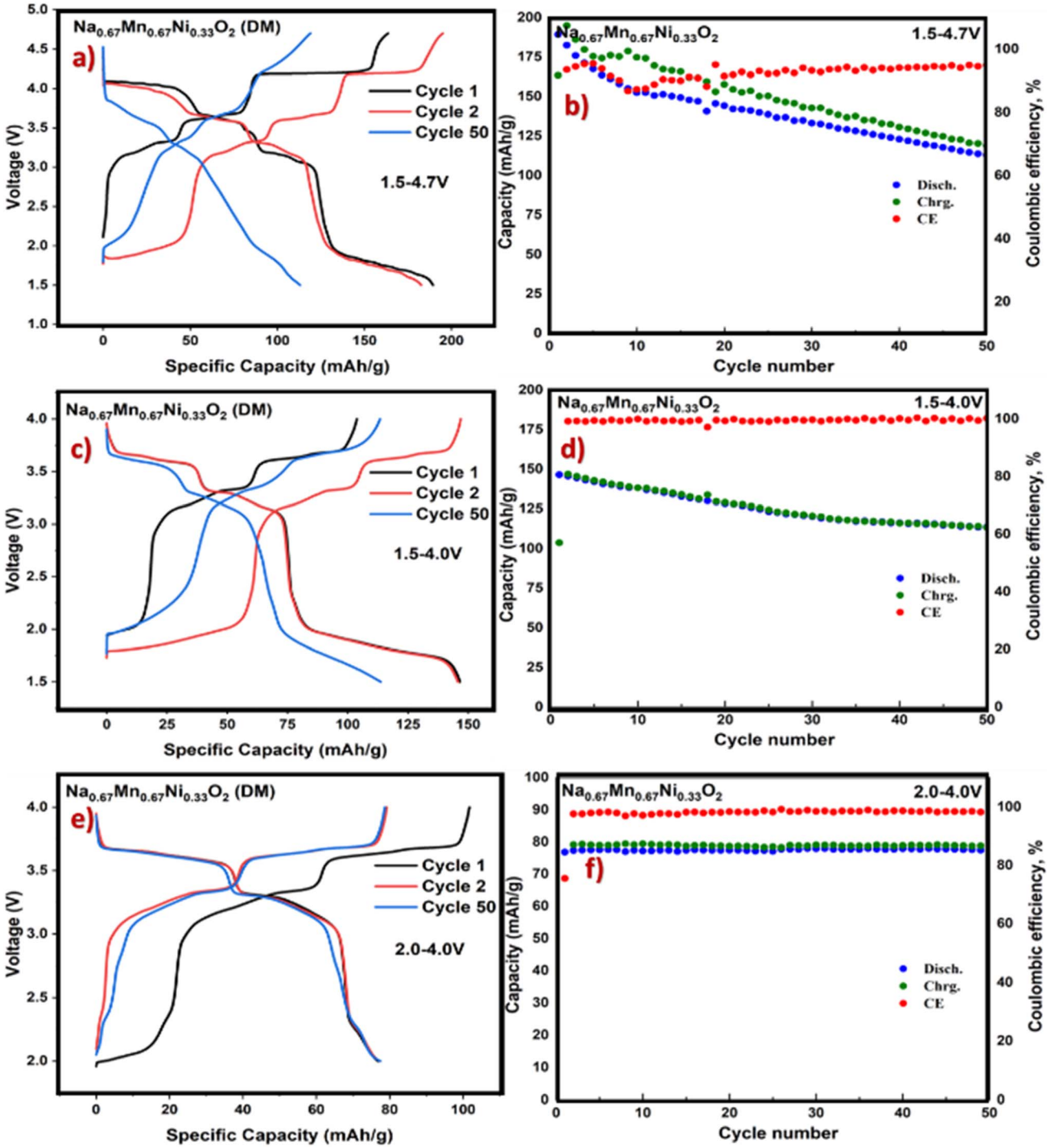

Fig. 5 Electrochemical performance of dry-milled (DM) $Na_{0.67}Mn_{0.67}Ni_{0.33}O_2$ electrodes: (a) initial charge–discharge profiles in the voltage range 1.5–4.7 V, (b) cycling stability at 1.5–4.7 V, (c & d) 1.5–4.0 V and (e & f) 2.0–4.0 V.

significantly enhanced, with the material maintaining approximately 86% of its capacity following 50 cycles as shown in Fig. 5d. The coulombic efficiency remained steady at almost 100% after the first cycle, signifying significant reversibility of the electrochemical reactions in this potential range. This stability shows that steering clear of extreme voltages successfully reduces unwanted side reactions and lessens irreversible phase alterations, thus maintaining the structural integrity of the cathode. Additional optimization was realized by limiting the operating window to 2.0–4.0 V as shown in Fig. 5e. Within this tighter range, the cathode demonstrated an initial discharge capacity of approximately 80 mA h g^{-1} and displayed exceptional cycling stability, with minimal capacity loss even after 50 cycles. Capacity retention approached 100%, and the

coulombic efficiency remained consistently high throughout cycling, underscoring the highly reversible nature of the redox processes in this voltage range (Fig. 5f). Overall, these results demonstrate that while extending the voltage window enables higher energy density, it severely compromises cycling stability due to irreversible structural and interfacial degradation. In contrast, operating within moderate voltage windows—particularly 1.5–4.0 V or 2.0–4.0 V—achieves a more practical balance between capacity and durability, establishing $Na_{0.67}Mn_{0.67}Ni_{0.33}O_2$ as a promising cathode candidate for long-life sodium-ion batteries.

The wet milling (WM) process initially enhanced the electrochemical performance of the $Na_{0.67}Mn_{0.67}Ni_{0.33}O_2$ electrode compared to the dry milling (DM) counterpart. As illustrated in Fig. 6a, the WM sample exhibited an outstanding initial discharge capacity of ~180 mA h g^{-1} within the 1.5–4.7 V window, significantly surpassing that of the DM electrode. This improvement can be attributed to the reduced particle size and enlarged surface area generated by wet milling, which promote superior electrode–electrolyte interfacial contact and facilitate faster sodium-ion diffusion and reaction kinetics. Despite this promising initial behavior, the long-term cycling stability of the WM electrode was markedly inferior. As shown in Fig. 6b and d, under both 1.5–4.7 V and 1.5–4.2 V windows, the WM electrode suffered from pronounced capacity fading, retaining only ~60–61% of its initial capacity after 50 cycles. In addition, the coulombic efficiency remained consistently lower and more unstable compared to the DM sample, further underscoring the poor reversibility of the electrochemical processes. The severe degradation highlights a critical trade-off introduced by wet milling: while the increased surface area accelerates electrochemical reactions and boosts the initial capacity, it simultaneously enhances electrode reactivity with the electrolyte, thereby intensifying parasitic side reactions, structural instability, and irreversible capacity loss. Consequently, although wet milling demonstrates advantages in terms of initial kinetics and capacity enhancement, it compromises long-term cycling durability, suggesting that an optimized balance between particle size reduction and surface stability is essential for achieving sustainable performance in Na-ion battery cathodes. Fig. 7 displays the SEM micrographs, elemental distribution maps, and EDS spectra of $Na_{0.67}Mn_{0.67}Ni_{0.33}O_2$ produced through dry milling and wet milling processes. Clear variations in particle shape and chemical uniformity are observable

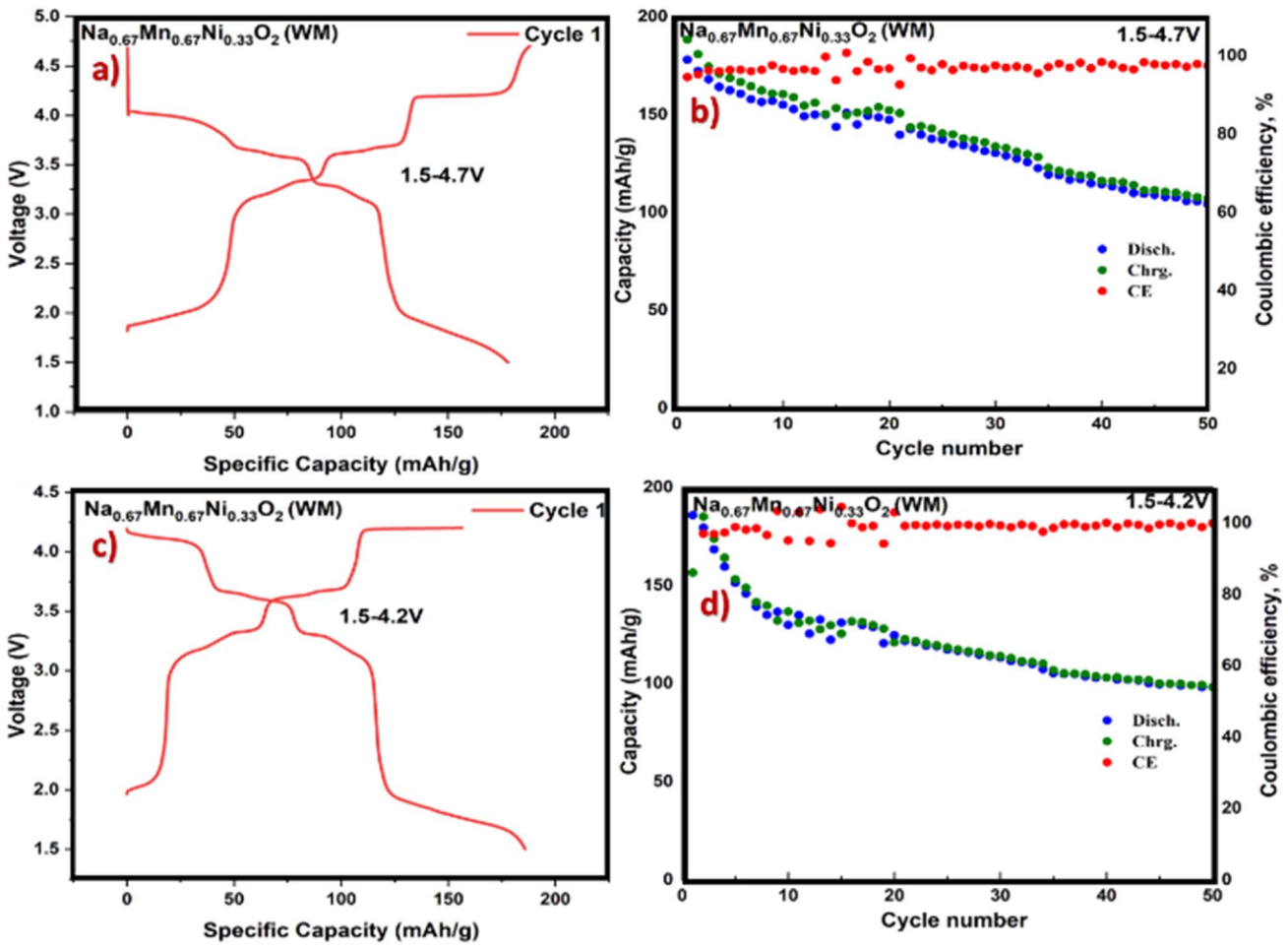

Fig. 6 Electrochemical performance of wet-milled (WM) $Na_{0.67}Mn_{0.67}Ni_{0.33}O_2$ electrodes: (a) initial charge–discharge profiles in the voltage range 1.5–4.7 V, (b) cycling stability at 1.5–4.7 V, (c & d) 1.5–4.2 V.

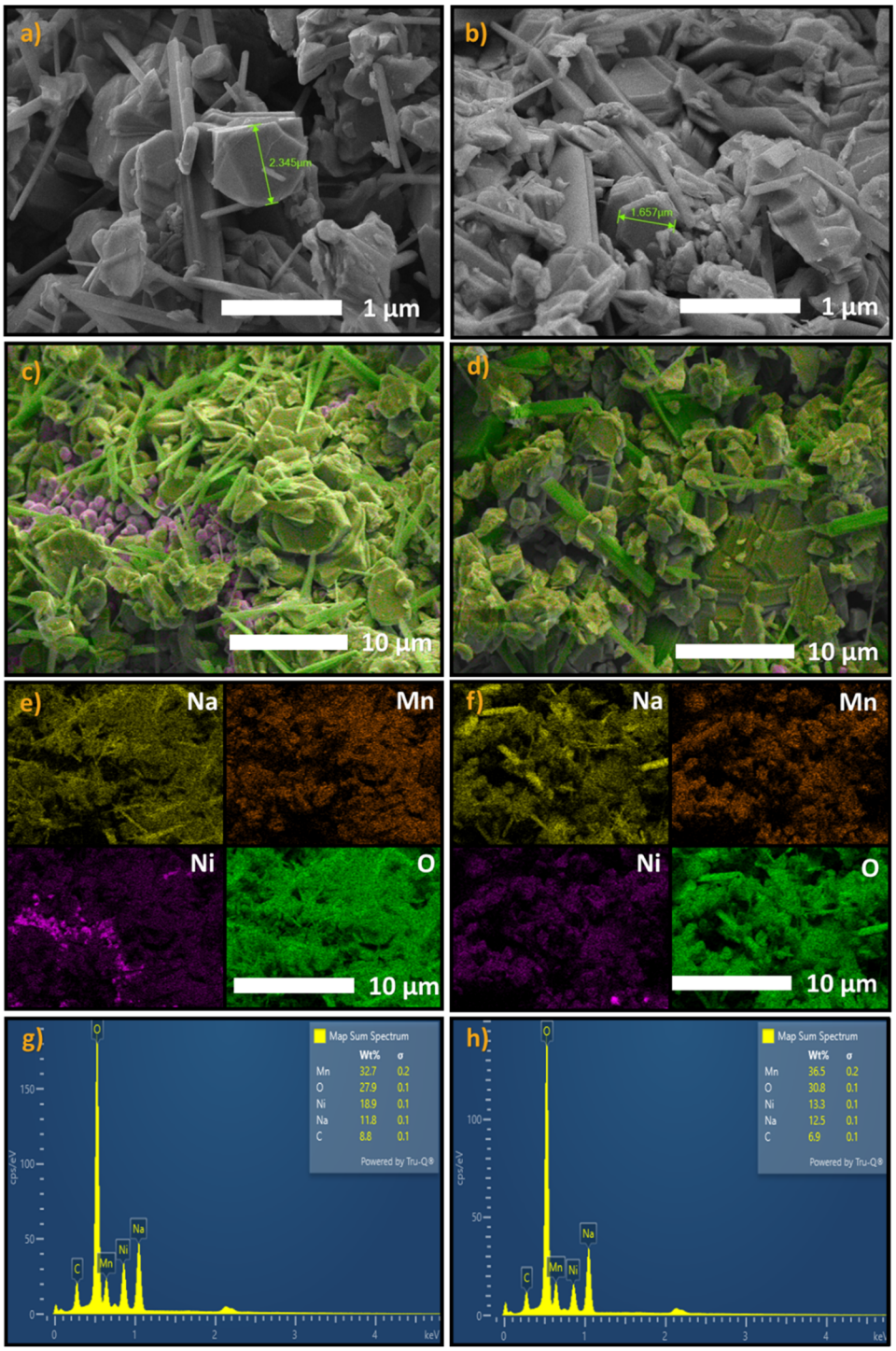

Fig. 7 SEM micrographs, elemental distribution maps, and EDS spectra of $Na_{0.67}Mn_{0.67}Ni_{0.33}O_2$ synthesized *via* dry milling (a, c, e and g) and wet milling (b, d, f and h).

between the two processing techniques. The dry-milled sample (Fig. 7a and c) shows noticeably larger grain sizes (~2.3 µm) in comparison to the wet-milled version (~1.6 µm, Fig. 7b and d). The dry-milled sample (Fig. 7a and c) shows noticeably larger grain sizes (~2.3 µm) in comparison to the wet-milled version (~1.6 µm, Fig. 7b and d). The grains in the dry-milled sample look less dense, whereas wet milling produces finer, more evenly spread grains. Elemental mapping provides additional evidence that Na, Mn, Ni, and O are found in the samples; however, the wet-milled specimen (Fig. 7f) shows a more uniform distribution of elements in contrast to the dry-milled sample (Fig. 7e), where minor segregation of Ni- and Na-rich areas is observable. The EDS quantification offers additional understanding of compositional variations. The wet-milled

sample exhibits a slightly lower Ni content (13.8 wt%) compared to the dry-milled sample (18.9 wt%), with marginally increased Mn and O contents. This variation indicates an incomplete reaction of Ni precursors during dry milling, resulting in remnants of unreacted NiO, which aligns with the previously discussed XRD analysis. The existence of unreacted NiO can function as an electrochemically inactive component, diminishing the total involvement of Ni redox couples throughout cycling. Notably, even with its bigger particle size and somewhat less uniform distribution, the dry-milled sample showed superior capacity retention during electrochemical testing, as previously mentioned. This enhanced stability can be linked to two main reasons: (i) the lack of unreacted NiO, allowing both Mn and Ni to engage in reversible redox reactions, and (ii) larger particle domains that decrease excessive surface reactivity with the electrolyte, thus lowering parasitic side reactions and improving long-term stability. In contrast, the wet-milled sample provides finer particles and better surface uniformity but is plagued by residual NiO, which diminishes active capacity and destabilizes structural integrity during repeated cycles. Consequently, the comparative assessment underscores that although wet milling enhances precursor mixing and reduces particle size, dry milling results in a more phase-pure layered oxide, which results in improved cycling stability.[35] The EDS and SEM findings support the electrochemical results, highlighting the necessity of balancing particle size reduction with full phase formation for optimal performance in sodium-ion battery cathodes. Fig. 8a illustrates the differential capacity (dQ/dV) curves of the $Na_{0.67}Mn_{0.67}Ni_{0.33}O_2$ electrodes produced through dry milling (DM) and wet milling (WM). Both electrodes exhibit unique redox peaks in the range of 2.0 to 4.0 V, aligning with the reversible Mn^{3+}/Mn^{4+} and Ni^{2+}/Ni^{4+} redox reactions that occur during Na^+ extraction and insertion. The existence of several peaks suggests a multi-step Na-ion intercalation process typical of layered oxides. The DM electrode shows more pronounced and sharper redox peaks than WM, particularly in the range of 3.3–3.6 V, alongside a smaller potential gap between the oxidation and reduction characteristics. This indicates reduced polarization and enhanced electrochemical reversibility, suggesting more effective Na-ion movement and redox processes. In comparison, the WM electrode displays wider and weaker peaks, suggesting slow kinetics and some overlap of redox reactions. The variations in peak sharpness and intensity can be attributed to the particle traits derived from the two milling techniques. Dry milling resulted in larger yet well-structured crystallites, promoting long-range Na-ion movement and decreasing grain boundary resistance, resulting in clearer redox signatures. Wet milling produces finer particles with increased surface area but also creates greater structural disorder and additional interfacial regions that could impede Na-ion mobility and expand the redox characteristics. This structural irregularity also amplifies electrode polarization, leading to reduced peak resolution. In general, the dQ/dV profiles indicate that the dry-milled electrode exhibits better redox reversibility and lower polarization than the wet-milled version, consistent with the previously presented capacity retention data. These findings validate that the synthesis method significantly influences the electrochemical characteristics of $Na_{0.67}Mn_{0.67}Ni_{0.33}O_2$, as dry milling leads to a more electrochemically advantageous microstructure.

Fig. 8b shows the comparison of both samples' (DM and WM) performance of the $Na_{0.67}Mn_{0.67}Ni_{0.33}O_2$ electrode with respect to rate capability under incremental current densities, returning afterward to the original low-rate state. At a baseline current density of 20 mA g^{-1}, the electrode provided a high and stable discharge capacity of approximately 190 mA h g^{-1} to

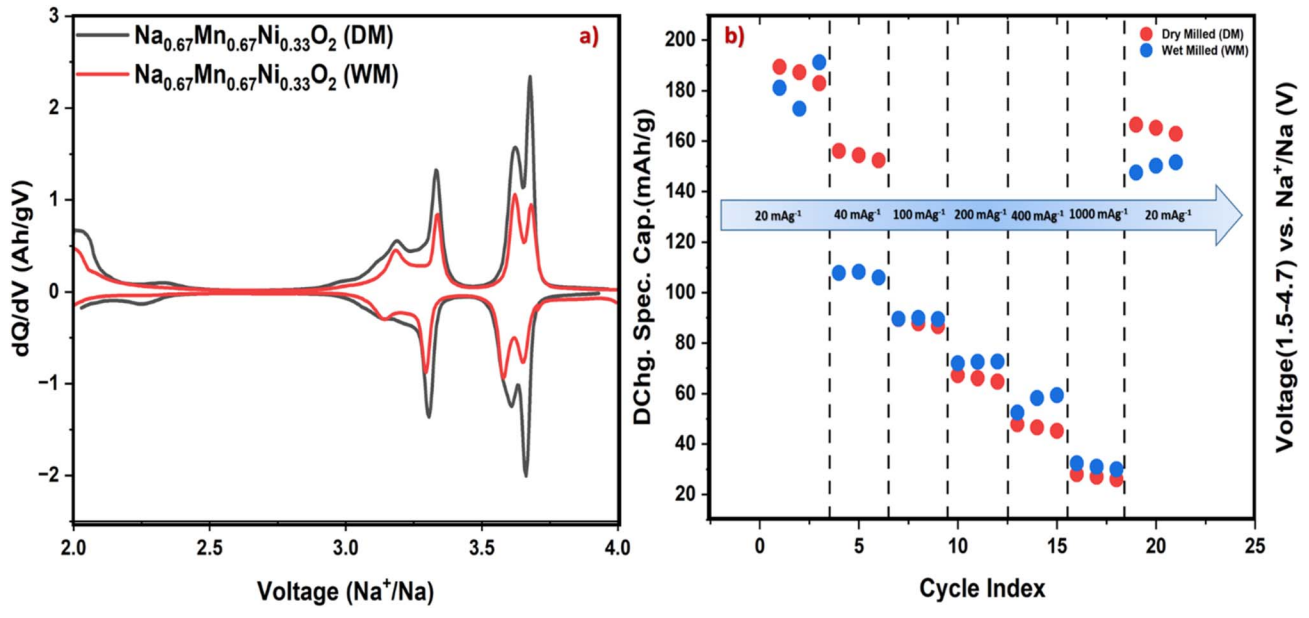

Fig. 8 (a) Differential capacity (dQ/dV) curves of $Na_{0.67}Mn_{0.67}Ni_{0.33}O_2$ electrodes synthesized by dry milling (DM) and wet milling (WM), (b) Rate capability of the dry-milled (DM) and wet milled (WM) $Na_{0.67}Mn_{0.67}Ni_{0.33}O_2$ electrode at various current densities.

198 mA h g^{-1}, respectively, aligning with the values recorded during galvanostatic cycling. Upon increasing the current density to 40 mA g^{-1}, the capacity experienced a minor decrease to approximately 156 mA h g^{-1} for the dry-milled sample while for the wet-milled sample, the capacity is 110 mA h g^{-1} suggesting effective Na^+ transport kinetics and minimal polarization in the dry-milled sample at moderate rates. At increased current densities, the anticipated capacity reduction became clearer: around 90 mA h g^{-1} at 100 mA g^{-1} and approximately 70 mA h g^{-1} at 200 mA g^{-1} for both methods. Similarly, the capacity dropped to about 28 mA h g^{-1} at 1000 mA g^{-1}, the most notable loss for dry and wet milled samples. The observed decrease suggests that there are kinetic restrictions on the mobility of Na^+ in the layered oxide structure and that the resistance is increased during fast charge–discharge operations. Significantly, the electrode regained almost all of its original capacity (~166 mA h g^{-1}) when the current density decreased to 20 mA g^{-1}. However, the wet-milled samples could not attain their former capacity when discharged at the same current density. This significant reversibility indicates that kinetic limitations, not prolonged structural deterioration, are responsible for the reduction in capacity seen at high rates. The remarkable rate performance of the dry-milled sample can be ascribed to its structured layered architecture, elevated crystallinity, and pure phases, which enhance long-range Na^+ movement and reduce grain boundary resistance. Although nanosized particles may enhance kinetics, they often exhibit increased surface reactivity and side reactions that threaten long-term stability. In comparison, the relatively larger, well-formed particle domains produced through the dry milling method achieve a suitable equilibrium. In contrast, the dry-milled structure mitigates these parasitic effects while maintaining sufficient transport kinetics, ensuring robust capacity retention and durability. The $Na_{0.67}Mn_{0.67}Ni_{0.33}O_2$ electrode, processed by dry milling, exhibits structural robustness and electrochemical reversibility as a cathode material based on the findings of rate capability. It shows promise for beneficial sodium-ion battery uses and confirms the effectiveness of the improved solid-state synthesis method by sustaining high capacities across a wide spectrum of current densities and nearly fully recuperating when reverting to low-rate functioning.

4 Conclusion

In this work, a phase-pure P2-type layered $Na_{0.67}Mn_{0.67}Ni_{0.33}O_2$ cathode material was successfully synthesized through an optimized solid-state reaction route. Comprehensive characterization using XRD, SEM, TEM, EDS, XPS, and ICP-OES confirmed its high crystallinity, ideal stoichiometry, and uniform Ni incorporation into the Mn–O framework without secondary phases. Electrochemical evaluation demonstrated a high initial discharge capacity of ~200 mA h g^{-1} within the wide voltage range of 1.5–4.7 V, along with excellent rate performance and long-term cycling stability. Ni replacement significantly improved reversibility and structural stability by reducing the Jahn–Teller distortions and alleviating voltage decay. The combined effects of Mn and Ni led to enhanced charge storage and long-lasting cycling stability. This research shows that $Na_{0.67}Mn_{0.67}Ni_{0.33}O_2$ is an exceptionally promising and scalable cathode material for future sodium-ion batteries, providing both efficiency and affordability.

Author contributions

Muhammad A. Jamali: experiments, characterisation, visualization, validation, writing – original draft. Bauyrzhan Myrzakhmetov: visualization, validation. Zhumabay Bakenov: writing – review & editing, visualization, validation, supervision, conceptualization. Aishuak Konarov: writing – review & editing, visualization, validation, supervision, resources, funding acquisition, conceptualization.

Conflicts of interest

The authors declare that they have no known competing financial interests or personal relationships that could have appeared to influence the work reported in this paper.

Data availability

All data supporting findings of this study are available within the article.

Acknowledgements

This work was funded by the Ministry of Science and Higher Education of the Republic of Kazakhstan Grant (AP22783602), by Nazarbayev University under Collaborative Research Program (Grant No. 20122022CRP1611, AK) and by Research Targeted Program "Development of new technologies of materials and energy storage systems for a green economy" BR21882402 from the Ministry of Science and Higher Education of the Republic of Kazakhstan. The authors also acknowledge the financial support from the INESS-2025 Organizing Committee and the Social Development Fund of Nazarbayev University, which covered the article processing charge for this publication.

References

1 R. M. Dell and D. A. J. Rand, *J. Power Sources*, 2001, **100**, 2–17, DOI: 10.1016/S0378-7753(01)00894-1.
2 K. R. Ngoy, V. T. Lukong, K. O. Yoro, J. B. Makambo, N. C. Chukwuati, C. Ibegbulam, O. Eterigho-Ikelegbe, K. Ukoba and T. C. Jen, *Renewable Sustainable Energy Rev.*, 2025, DOI: 10.1016/j.rser.2025.115971.
3 T. P. Narins, *Extr. Ind. Soc.*, 2017, **4**, 321–328, DOI: 10.1016/j.exis.2017.01.013.
4 C. Delmas, *Adv. Energy Mater.*, 2018, **8**, 1703137, DOI: 10.1002/aenm.201703137.
5 N. Ortiz-Vitoriano, N. E. Drewett, E. Gonzalo and T. Rojo, *Energy Environ. Sci.*, 2017, **10**, 1051–1074, DOI: 10.1039/C7EE00566K.

6 S. Zhang, B. Steubing, H. Karlsson Potter, P. A. Hansson and Å. Nordberg, *Resour. Conserv. Recycl.*, 2024, **202**, 107362, DOI: 10.1016/j.resconrec.2023.107362.
7 A. R. Nurohmah, S. S. Nisa, K. N. R. Stulasti, C. S. Yudha, W. G. Suci, K. Aliwarga, H. Widiyandari and A. Purwanto, *Mater. Renew. Sustain. Energy*, 2022, **11**, 71–89, DOI: 10.1007/s40243-022-00208-1.
8 J.-Y. Hwang, S.-T. Myung and Y.-K. Sun, *Chem. Soc. Rev.*, 2017, **46**, 3529–3614, DOI: 10.1039/C6CS00776G.
9 A. Namazbay, M. Karlykan, L. Rakhymbay, Z. Bakenov, N. Voronina, S.-T. Myung and A. Konarov, *Energy Storage Mater.*, 2025, **77**, 104212, DOI: 10.1016/j.ensm.2025.104212.
10 L. Zhao, T. Zhang, W. Li, T. Li, L. Zhang, X. Zhang and Z. Wang, *Engineering*, 2023, **24**, 172–183, DOI: 10.1016/j.eng.2021.08.032.
11 H. Rostami, J. Valio, P. Suominen, P. Tynjälä and U. Lassi, *Chem. Eng. J.*, 2024, **495**, 153471, DOI: 10.1016/j.cej.2024.153471.
12 N. Hong, K. Wu, Z. Peng, Z. Zhu, G. Jia and M. Wang, *J. Phys. Chem. C*, 2020, **124**(42), 22925–22933, DOI: 10.1021/acs.jpcc.0c06032.
13 R. Usiskin, Y. Lu, J. Popovic, *et al*, *Nat Rev Mater*, 2021, **6**, 1020–1035, DOI: 10.1038/s41578-021-00324-w.
14 J. Tang, A. D. Dysart and V. G. Pol, *Curr. Opin. Chem. Eng.*, 2015, **9**, 34–41, DOI: 10.1016/j.coche.2015.08.007.
15 E. J. Kim, R. Tatara, T. Hosaka, K. Kubota, S. Kumakura and S. Komaba, *ACS Appl. Energy Mater.*, 2024, **7**, 1015–1026, DOI: 10.1021/acsaem.3c02462.
16 P. Phogat, S. Dey and M. Wan, *Mater. Sci. Eng., B*, 2025, **312**, 117870, DOI: 10.1016/j.mseb.2024.117870.
17 H. Ge, F. Kong, S. Jiang, H. Huang, D. J. He, X. Huang, X. Mu and H. Xia, *Energy Storage Mater.*, 2025, **81**, 104468, DOI: 10.1016/j.ensm.2025.104468.
18 J. Peng, W. Hua, Z. Yang, J. Y. Li, J. Wang, Y. Liang, L. Zhao, W. Lai, X. Wu, Z. Cheng, G. Peleckis, S. Indris, J. Z. Wang, H. K. Liu, S. X. Dou and S. Chou, *ACS Nano*, 2024, **18**, 19854–19864, DOI: 10.1021/acsnano.4c07021.
19 J. Lu, J. Zhang, Y. Huang, Y. Zhang, Y. Yin and S. Bao, *Front. Energy Res.*, 2023, **11**, 1–10, DOI: 10.3389/fenrg.2023.1246327.
20 A. Konarov, H. J. Kim, N. Voronina, Z. Bakenov and S.-T. Myung, *ACS Appl. Mater. Interfaces*, 2019, **11**, 28928–28933, DOI: 10.1021/acsami.9b09317.
21 C. Wu, Y. Xu, J. Song, Y. Hou, S. Jiang, R. He, A. Wei and Q. Tan, *Chem. Eng. J.*, 2024, **500**, 157264, DOI: 10.1016/j.cej.2024.157264.
22 B. Shugay, L. Rakhymbay, A. Konarov, S.-T. Myung and Z. Bakenov, *Electrochem. Commun.*, 2023, **146**, 107413, DOI: 10.1016/j.elecom.2022.107413.
23 N. Voronina, H. J. Kim, A. Konarov, N. Yaqoob, K.-S. Lee, P. Kaghazchi, O. Guillon and S.-T. Myung, *Adv. Energy Mater.*, 2021, **11**, 2003399, DOI: 10.1002/aenm.202003399.
24 N. Voronina, J. H. Yu, H. J. Kim, N. Yaqoob, O. Guillon, H. Kim, M. Jung, H. Jung, K. Yazawa, H. Yashiro, P. Kaghazchi and S. Myung, *Adv. Funct. Mater.*, 2023, **33**, 2210423, DOI: 10.1002/adfm.202210423.
25 Y. Huang, W. Zeng, K. Li and X. Zhu, *Microstructures*, 2024, **4**, 2024027, DOI: 10.20517/microstructures.2023.102.
26 L. Rakhymbay, A. Namazbay, M. Karlykan, M. Abilkairova, A. Konarov and Z. Bakenov, *Int. J. Electrochem. Sci.*, 2022, **17**, 221234, DOI: 10.20964/2022.12.28.
27 S. Kumakura, Y. Tahara, K. Kubota, K. Chihara and S. Komaba, *Angew. Chem., Int. Ed.*, 2016, **55**, 12760–12763, DOI: 10.1002/anie.201606415.
28 E. J. Kim, T. Hosaka, K. Kubota, R. Tatara, S. Kumakura and S. Komaba, *ACS Appl. Energy Mater.*, 2022, **5**, 12999–13010, DOI: 10.1021/acsaem.2c02581.
29 H. Li, W. Zhang, K. Sun, J. Guo, K. Yuan, J. Fu, T. Zhang, X. Zhang, H. Long, Z. Zhang, Y. Lai and H. Sun, *Adv. Energy Mater.*, 2021, **11**, 1–35, DOI: 10.1002/aenm.202003154.
30 L. Dai, Y. Wang, L. Sun, Y. Ding, Y. Yao, L. Yao, N. E. Drewett, W. Zhang, J. Tang and W. Zheng, *Adv. Sci.*, 2021, **8**, 1–10, DOI: 10.1002/advs.202004995.
31 L. Rakhymbay, Z. Zhakiyeva, J. Ho Yu, A.-Y. Kim, H.-G. Jung, Z. Bagindyk, Z. Bakenov, S.-T. Myung and A. Konarov, *J. Mater. Chem. A*, 2025, **13**, 6697–6708, DOI: 10.1039/D4TA07432G.
32 Y. J. Li, Y. F. Zhu, B. B. Chen, X. B. Jia, H. Xin, G. Z. Zhao, G. Zhu, S. X. Dou and Y. Xiao, *Adv. Funct. Mater.*, 2025, **2504096**, 1–32, DOI: 10.1002/adfm.202504096.
33 S. Lavela, A. C. do N. Santos, F. V. da Motta, M. R. D. Bomio, P. Lavela, C. Pérez Vicente and J. L. Tirado, *ACS Appl. Mater. Interfaces*, 2024, **16**, 56975–56986, DOI: 10.1021/acsami.4c09706.
34 K. Wu, P. Ran, X. Zhang, Y. Zhang and B. Liu, *ACS Appl. Energy Mater.*, 2025, **8**, 12071–12082, DOI: 10.1021/acsaem.5c01568.
35 E. J. Kim, R. Tatara, T. Hosaka, K. Kubota, S. Kumakura and S. Komaba, 2024, 0–11. DOI: 10.1021/acsaem.3c02462.
36 M. Almazrouei, S. Park, M. Houck, M. De Volder, S. Hochgreb and A. Boies, *ACS Appl. Mater. Interfaces*, 2024, **16**, 33633–33646, DOI: 10.1021/acsami.4c06503.
37 C. A. Downes, K. M. Van Allsburg, S. A. Tacey, K. A. Unocic, F. G. Baddour, D. A. Ruddy, N. J. Libretto, M. M. O'Connor, C. A. Farberow, J. A. Schaidle and S. E. Habas, *Chem. Mater.*, 2022, **34**, 6255–6267, DOI: 10.1021/acs.chemmater.2c00085.
38 Y. Ma, Z. Wu, H. Wang, G. Wang, Y. Zhang, P. Hu, Y. Li, D. Gao, H. Pu, B. Wang and X. Qi, *CrystEngComm*, 2019, **21**, 3982–3992, DOI: 10.1039/c9ce00495e.
39 X. Zhao, W. Wu, Y. Bai, Y. Wu, J. Liu, P. Wang, H. Luo, K. Ren, Y. Song, H. Du and J. Deng, *J. Power Sources*, 2024, **613**, 234913, DOI: 10.1016/j.jpowsour.2024.234913.
40 W. Zuo, A. Innocenti, M. Zarrabeitia, D. Bresser, Y. Yang and S. Passerini, *Acc. Chem. Res.*, 2023, **56**, 284–296, DOI: 10.1021/acs.accounts.2c00690.